

Article

Critical Influence of Redox Pretreatments on the CO Oxidation Activity of BaFeO₃-# Perovskites: An In-Depth Atomic Scale Analysis by Aberration-Corrected and In-Situ Diffraction Techniques

Achraf el Hadri, Isabel Gómez-Recio, Eloy del Rio, Juan C. Hernandez-Garrido, Raquel Cortés-Gil, María Hernando, Áurea Varela, Angel Gutierrez-Alonso, Marina Parras, Juan J. Delgado, José A. Pérez-Omil, Ginesa Blanco, José J. Calvino, and Jose M. Gonzalez-Calbet

ACS Catal., Just Accepted Manuscript • DOI: 10.1021/acscatal.7b02595 • Publication Date (Web): 07 Nov 2017

Downloaded from <http://pubs.acs.org> on November 7, 2017

Just Accepted

“Just Accepted” manuscripts have been peer-reviewed and accepted for publication. They are posted online prior to technical editing, formatting for publication and author proofing. The American Chemical Society provides “Just Accepted” as a free service to the research community to expedite the dissemination of scientific material as soon as possible after acceptance. “Just Accepted” manuscripts appear in full in PDF format accompanied by an HTML abstract. “Just Accepted” manuscripts have been fully peer reviewed, but should not be considered the official version of record. They are accessible to all readers and citable by the Digital Object Identifier (DOI®). “Just Accepted” is an optional service offered to authors. Therefore, the “Just Accepted” Web site may not include all articles that will be published in the journal. After a manuscript is technically edited and formatted, it will be removed from the “Just Accepted” Web site and published as an ASAP article. Note that technical editing may introduce minor changes to the manuscript text and/or graphics which could affect content, and all legal disclaimers and ethical guidelines that apply to the journal pertain. ACS cannot be held responsible for errors or consequences arising from the use of information contained in these “Just Accepted” manuscripts.



ACS Publications

ACS Catalysis is published by the American Chemical Society. 1155 Sixteenth Street N.W., Washington, DC 20036

Published by American Chemical Society. Copyright © American Chemical Society. However, no copyright claim is made to original U.S. Government works, or works produced by employees of any Commonwealth realm Crown government in the course of their duties.

1
2
3
4
5
6
7
8
9
10
11
12
13
14
15
16
17
18
19
20
21
22
23
24
25
26
27
28
29
30
31
32
33
34
35
36
37
38
39
40
41
42
43
44
45
46
47
48
49
50
51
52
53
54
55
56
57
58
59
60

Critical Influence of Redox Pretreatments on the CO Oxidation Activity of BaFeO_{3-δ} Perovskites: An In-Depth Atomic Scale Analysis by Aberration-Corrected and *In-Situ* Diffraction Techniques

Achraf el Hadri¹, Isabel Gómez-Recio¹, Eloy del Río^{2,3}, Juan C. Hernández-Garrido^{2,3}, Raquel Cortés-Gil¹, María Hernando¹, Áurea Varela¹, Ángel Gutiérrez-Alonso¹, Marina Parras¹, Juan J. Delgado^{2,3}, José A. Pérez-Omil^{2,3}, Ginesa Blanco^{2,3}, José J. Calvino^{2,3}, José M. González-Calbet^{1,4*}

¹Departamento de Química Inorgánica. Facultad de Ciencias Químicas. Universidad Complutense, 28040-Madrid, Spain

²Departamento de Ciencia de los Materiales e Ingeniería Metalúrgica y Química Inorgánica. Facultad de Ciencias. Universidad de Cádiz. Campus Río San Pedro, 11510-Puerto Real, Spain

³Instituto Universitario de Investigación en Microscopía Electrónica y Materiales (IMEYMAT). Facultad de Ciencias. Universidad Complutense, Campus Río San Pedro, 11510-Puerto Real, Spain

⁴Centro Nacional de Microscopía Electrónica. Universidad Complutense, 28040-Madrid, Spain

ABSTRACT: A BaFeO_{3-δ} ($\delta \approx 0.22$) perovskite was prepared by a sol-gel method and essayed as catalyst in the CO oxidation reaction. BaFeO_{3-δ} ($0.22 \leq \delta \leq 0.42$) depicts a 6H perovskite hexagonal structural type with Fe in both (III) and (IV) oxidation state and oxygen stoichiometry accommodated by random distribution of anionic vacancies. The perovskite with the highest oxygen content, BaFeO_{2.78}, proved to be more active than its lanthanide-based counterparts, LnFeO₃ (Ln=La, Sm, Nd). Removal of the lattice oxygen detected in both Temperature Programmed Oxidation (TPO) and Reduction (TPR) experiments at around 500 K, and which leads to the complete reduction of Fe⁴⁺ to Fe³⁺, i.e. to a BaFeO_{2.5}, decreases significantly the catalytic activity, especially in the low temperature range. The analysis of thermogravimetric experiments performed under oxygen and of TPR studies run under CO clearly support the involvement of lattice oxygen in the CO oxidation on these Ba-Fe perovskites, even at the lowest temperatures. Atomically resolved images and chemical maps obtained using different Aberration-Corrected Scanning Transmission Electron Microscopy techniques, as well as some *in-situ* type experiments, have provided a clear picture of the accommodation of oxygen-non-stoichiometry in these materials. This atomic-scale view has revealed details of both the cation and anion sublattices of the different perovskites that have allowed us identifying the structural origin of the oxygen species most likely responsible of the low temperature CO oxidation activity.

KEYWORDS: *Ba-Fe Perovskites, Oxygen vacancies, CO Oxidation, Activation Pretreatments, Aberration-Corrected Electron Microscopy, In-Situ Diffraction Techniques*

INTRODUCTION

The substitution of so-called critical elements, among which Noble Metals (NM) and some Rare Earths (RE) are included, has become a question of major concern to reach the goal of sustainable development.⁽¹⁻³⁾ Thus, eliminating or reducing the amounts used of these elements in the preparation of materials involved in their different applications, is not just, as in the most recent past, a matter of an improved economy but, more importantly, of guaranteeing their availability to fully develop Green Technologies. In the particular context of Heterogeneous Catalysis, the substitution of NM by Transition, mostly 3d, Metals,

is an issue that has already received attention.⁽⁴⁾ In connection with this target, AMO₃ related perovskites, have been essayed as catalysts in a number of reactions, most of them redox processes.⁽⁴⁻¹¹⁾ As compared to the corresponding MO_x oxides, the high flexibility of the perovskite structure offers much more opportunities to tailor the oxidation state and the characteristics of the oxygen environment of the catalytically active M element, while preserving a high thermal stability. Thus, by appropriate substitution in the A and M sublattices or both, a variety of materials can be produced, A_xA' _{1-x}M_yM' _{1-y}O_{3-z}, in which M oxidation state and anionic deficiency can be modulated with some modifications of the basic structure. These controlled

1 changes can be used to modify the physical and chemical response of the solid, e.g. its catalytic behavior.

2
3 Lanthanide based Fe, Mn and Co perovskites,
4 LnMO_3 (Ln =lanthanide, M=Fe, Co, Mn), have been
5 the most studied systems, particularly as catalysts in
6 the CO oxidation reaction. The initial interest in this
7 particular process stemmed from applications in auto-
8 motive pollution control devices⁽¹²⁻²¹⁾ but, more re-
9 cently, has turned towards the production of hydrogen
10 for fuel cells. Among them, LaCoO_3 shows the best
11 performance in CO oxidation, especially when care is
12 taken during the synthesis to obtain a sample with me-
13 dium surface area and good surface crystallinity.⁽²²⁾ $\text{La}-$
14 FeO_3 has been reported to be less active than Mn- or
15 Co-based perovskites but they seem to present im-
16 proved stability under working conditions,⁽⁷⁾ partic-
17 ularly in reactions involving high temperatures and oxi-
18 dizing environments.⁽²³⁾

19 Substitution of La by an alkaline earth⁽²⁴⁻²⁷⁾ has
20 been reported to significantly modify the catalytic ac-
21 tivity of LnMO_3 perovskites, the modification de-
22 pending on the M element, the amount of the alkaline
23 earth addition and, of course, the particular reaction.
24 To balance the charge deficiency produced by the in-
25 corporation of divalent ions into the A sublattice, the
26 M element increases its average oxidation state, oxy-
27 gen vacancies are created or both things occur sim-
28 taneously. This is the case of Co and Fe perovskites, for
29 which a small fraction of vacancies appear and the
30 $\text{M}^{4+}/\text{M}^{3+}$ ratio increases in parallel with the alkaline
31 earth content.

32 In the case of Ba substitution, to the best of our
33 knowledge, no data are currently available concerning
34 the effects of Ba substitution on CO oxidation. More-
35 over, studies available of the totally substituted Ba per-
36 ovskites, $\text{BaFeO}_{3-\delta}$, refer mostly to its CO_2 absorption
37 capabilities.⁽²⁸⁻²⁹⁾ As these last papers evidence, the to-
38 tal substitution of La^{3+} by Ba^{2+} may not only change
39 the redox response of the solid but also its basic char-
40 acter, a factor which may influence the catalytic behav-
41 ior in reactions, as it is the case of CO oxidation, where
42 one of the products (CO_2) has acid character.

43 Total substitution of La by Ba fits perfectly with the
44 actual demands to replace critical RE, as it is the case

45 of La. However, from the perspective of catalytic ap-
46 plications, only Xian *et al* have recently studied the
47 NO_x storage capacity (NSC) of $\text{BaFeO}_{3-\delta}$ perovskites.
48 In their work, they found an influence of both the final
49 calcination temperature used during the synthesis of
50 the solid and the temperature at which NSC was meas-
51 ured.⁽³⁰⁻³²⁾ The functional behavior was in this case
52 characterized after pretreating the different solids at
53 773 K, but the exact influence of the pretreatment
54 temperature was not considered. In our view, this is a
55 critical aspect since, as we will prove here, the choice
56 of this temperature may significantly influence the
57 structure of the oxygen sublattice, leading to solids
58 with different total oxygen contents and, concomitantly,
59 different chemical responses. In fact, the
60 $\text{BaFeO}_{3-\delta}$ system is able to stabilize several non-sto-
61 chiometric perovskite related structures with $0.1 \leq \delta \leq$
62 0.5.⁽³³⁾ At this point, it is worth recalling that a fast
63 transport pathway has recently been attributed to the
64 non-stoichiometry of $(\text{La}_{0.8}\text{Sr}_{0.2})_{0.95}\text{MnO}_{3+\delta}$.⁽³⁴⁾ Oxy-
65 gen non-stoichiometry is, in this case, accompanied by
66 a variation in the average $\text{Fe}^{4+}/\text{Fe}^{3+}$ ratio. The fully sto-
67 chiometric, 100% Fe^{4+} , compound, BaFeO_3 has only
68 been synthesized by low temperature oxidation using
69 ozone.⁽³⁵⁾ It is important to state that the content in
70 highly oxidized Fe^{4+} species has been pointed out as
71 responsible of the catalytic activity observed in $\text{La}-$
72 $\text{Fe}_x\text{Ni}_{1-x}\text{O}_{3+\delta}$ oxides in the H_2O_2 decomposition reac-
73 tion.⁽³⁶⁻³⁸⁾ Its role in the performance of $\text{BaFeO}_{3-\delta}$ be-
74 comes therefore a question to check.

75 From a mechanistic point of view, CO oxidation on
76 perovskites is generally accepted^(5-8,12,13,15) to proceed
77 through so-called *suprafacial* catalysis, at least at the
78 lowest temperatures (below 673 K). In the suprafacial
79 process, which could also be alternatively termed as a
80 Langmuir-Hinselwood mechanism, the role of the
81 outermost surface is providing the atomic orbitals of
82 proper symmetry for adsorption and intermolecular
83 reactions of the reactants involved, this explaining the
84 trends observed in the variations of catalytic activity
85 with the total occupation of the *d* orbitals of the M
86 metal, which is the one considered as the active com-
87 ponent. This mechanism would change to an intra-
88 facial one at the highest temperatures. The intrafacial
89 catalysis, a Mars-Krevelen alike mechanism, consists

in a redox cycle mediated by the lattice oxygen of the perovskite. The presence of oxygen vacancies and high oxygen mobility are considered the factors that favour this intrafacial route.

In spite of this simplistic distinction, different authors support the occurrence of the intrafacial mechanism even at the lowest temperatures.^(16,24,28-33,35-38) Moreover, L. Yamada *et al*^(16,35-39) have reported that the exact electronic structure of “Fe⁴⁺” species in Sr-Fe and Ba-Fe perovskites (SFOs and BFOs respectively) cannot be understood in terms of pure *d* orbitals occupation, but instead as an interplay between Fe *d* electrons and O *p* holes. The electronic structure of these solids differs substantially from the picture of localized-electrons depicted by the supra/intrafacial interpretation, which would only appear appropriate for the un-substituted oxide. From this perspective, it does not seem that straightforward to differentiate between the electronic state of iron in the structure and the properties of the oxygen sublattice, both being in fact correlated. Moreover, although there is no data available, it is very likely that the strength of such correlation will possibly change with the exact oxygen content of the solid.

Taking into account all these comments, we have considered of interest exploring the catalytic behavior of a, lanthanide-free, BaFeO_{3-δ} perovskite in CO oxidation, putting emphasis on the influence of the redox pretreatments on catalytic activity and on the possible involvement of lattice oxygen in the process. An important aspect to stress at this point is that, to avoid the influence of changes in textural properties, we have performed this study starting from a single solid, prepared by calcination at 1073 K, and then modulating the oxygen content by appropriate treatments under H₂ at temperatures further below the calcination temperature and which, therefore, did not produce any significant sintering. This approach neatly differs from that followed in previous works in which the influence of oxygen content was studied by preparing solids at different calcination temperatures.⁽⁴⁰⁾ In this last case, catalysts with final surface areas differing in a large percent were obtained, this making any further catalytic activity comparison rather cumbersome.

Finally, it is worth mentioning that in spite of being widely admitted, since long, that the catalytic behavior

of perovskites is intimately related to the nature of their defect structure, studies particularly focused on the detailed analysis of the exact nature of such defects at atomic scale are systematically lacking. The structural characterization techniques involved in the literature dealing with catalysis by perovskites limits mostly to X-Ray powder diffraction (XRD) and X-Ray photoelectron spectroscopy (XPS).^(5,8)

This clearly contrasts with the systematic and widespread use of Scanning-Transmission Electron Microscopy (STEM) based techniques as tools to correlate the atomic scale structural details of perovskites with their physical properties. Such an evident under-exploitation of the capabilities of this family of techniques is especially hard to understand nowadays when the recent development of novel electron-optical elements, such as lens aberration correctors allowed the development of different techniques which render structural and analytical information at atomic-column spatial resolution.^(41,42)

To illustrate the large potential of the STEM techniques available in these modern aberration-corrected microscopes, as a source of structural data to rationalize the catalytic behavior of perovskites, we have performed a thorough characterization of both the cation and anion sublattices of the materials investigated, combining a variety of STEM techniques. Some of these experiments were performed using an *in-situ* heating stage inside the microscope chamber in order to follow the influence of activation temperature on structure. From the whole set of results obtained in this atomic-scale analysis it has been possible to establish a relationship between catalytic activity and structural features of BaFeO_{3-δ} perovskites.

EXPERIMENTAL SECTION

The BaFeO_{3-δ} catalyst was prepared by a sol-gel method. Thus, stoichiometric amounts of Ba(NO₃)₂ (Merck, 99%) and Fe(NO₃)₃.9H₂O (Acros Organics, 99,9%) were dissolved in distilled water. Citric acid (C₆H₈O₇, Sigma Aldrich, 99,5%), CA, and ethylene glycol (C₂H₆O₂, Sigma Aldrich, 99,8%), EG, were then added under stirring at 323 K constant temperature. A CA: EG molar ratio of 2:40 was used for the synthesis. The resulting solution was further condensed heating on a hot plate around 400 K until the corresponding

gel was formed. The resulting solid was then heated in air at 623 K for 22 hours in order to decompose nitrates and to remove the organic moieties. The calcination temperature was raised up to 1073 K and maintained during 24 hours. The final step consisted in a fast quenching in air to room temperature.

XRD patterns were recorded in an X'PERT-MPD diffractometer equipped with an X-Ray source working with Cu K α radiation at 45 kV and 40 mA. Patterns were recorded in the 10°- 80° 2 θ range, using a step size of 0.04° and an integration time of 1 s at each step. A high temperature chamber, Anton Paar HTK2000, was used for XRD diffraction under heating conditions in the 273-673 K temperature range. XRD patterns were recorded in the 20°-80° range, using a step size of 0.033° and a collection time of 100 s with X'Celerator fast detector at each step. All XRD patterns were gathered up each 100 and 50 K in heating and cooling conditions, respectively.

Neutron Powder diffraction (NPD) analysis was performed at the Institut Laue Langevin Grenoble, France on the D2B diffractometer ($\lambda=0.1594$ nm). The data were analyzed with the Rietveld method using the software package FullProf.⁽⁴³⁾

X-ray Photoelectron Spectra were obtained on a Kratos Axis Ultra DLD instrument, and recorded with monochromatic Al K α radiation (1486.6 eV). The instrument was operated in the fixed analysis transmission mode (FAT), using pass energy of 20 eV for the high resolution areas. The Kratos coaxial charge neutralization system was used to compensate charging effects. Data analysis was performed by using CasaXPS software (version 2.3.18dev1.1l).

For electron microscopy characterization, a variety of equipment was used. Scanning electron microscopy (SEM) has been carried out in a JEOL 6335 FEG scanning electron microscope. Basic structural characterization was performed on a JEOL JEM 300FEG electron microscope whereas atomic scale characterization was done in a JEOL JSM-ARM200cF microscope (Cold Emission Gun) operated at 200 kV provided with a spherical aberration corrector in probe (current emission density $\sim 1.4 \times 10^9$ A and probe size ~ 0.8 Å), a GIF-QuantumER™ spectrometer and Oxford INCA-350 detector. Solid semi-angles between 90-

370 mrad and 11-22 mrad were used for acquisition of HAADF (high angle annular dark field) and ABF (annular bright field) images, respectively (38 s per frame). Electron energy loss spectroscopy (EELS) maps were acquired with a spatial resolution ~ 0.4 Å, over a total acquisition time ~ 2 min (current emission density of $\sim 1.2 \times 10^{-8}$ A and a probe size of ~ 1.2 Å). Principal Component Analysis⁽⁴⁴⁾ was performed on EELS data set to de-noise the spectra by using the Hyperspy data analysis toolbox.⁽⁴⁵⁾ Chemical maps were constructed selecting the elements to identify and considering the experimental conditions (beam energy, convergence and collection semi-angles). Power-law background subtraction was used for the selected spectrum and all the edge setup applied to the parent spectrum imaging.⁽⁴⁶⁾

BET surface area was determined by N₂ physisorption at 77 K using Micromeritics ASAP-2020 automatic equipment.

The average cationic composition was determined by energy dispersive x-ray spectroscopy (EDS). The average oxidation state of iron was determined by a redox titration method. Samples were dissolved in HCl (6 N) with an excess of Mohr salt. The Fe²⁺ ions react with the possible Fe⁴⁺ present in the sample leading to Fe³⁺ ions. The amount of remaining Fe²⁺ ions is determined by titration with a 0.1 N K₂Cr₂O₇ solution.

Thermogravimetric analysis (TGA) was performed using a Cahn D-200 electro-balance and a TG/DTA 6300 SII EXSTAR. Oxygen content determination was done measuring the weight loss under H₂. In these experiments, 50 mg of the sample were heated inside a Pt crucible, at a constant rate of 6 K/minute up to 1173 K, under a static atmosphere at 0.2 bar H₂ / 0.3 bar He.

Temperature Programmed Reduction (TPR) and Oxidation (TPO) experiments were performed in an experimental setup coupled to a Pfeiffer Vacuum, model Thermostar GSD301T1, quadrupole mass spectrometer. In all these experiments, 50 mg of the sample were submitted to a surface cleaning pretreatment under O₂(5%)/He at 523 K for 1 h and further cooled down to room temperature under the same atmosphere. For the H₂-TPR essays, the catalysts were heated in a quartz micro reactor under a 60 cm³/min

flow of H₂(5%)/Ar from room temperature up to 1173 K at a constant heating rate of 10 K/min. The same pretreatment, flow and heating conditions were used for CO-TPR and TPO experiments but a gas mixture of CO(5%)/He and O₂(5%)/He were used respectively instead.

CO oxidation tests were run in a tubular quartz micro reactor. In these essays, 25 mg of the samples were mixed with 100 mg of finely crushed quartz in order to avoid the formation of hot spots in the catalytic bed during the reaction. The feed gas composition was the following: 1% CO, 0.6% O, 98.4% He. A 100 cm³/min flow velocity under atmospheric pressure was adjusted through Bruker model Bronkhorst mass-flow controllers. These conditions correspond to a total space velocity of 240,000 cm³/h·g. CO conversion and CO₂ formation were continuously monitored using a Pfeiffer, mass spectrometer, model QME-200 D-35614, while the catalyst was heated under the reactant mixture from room temperature up to 1073 K at a constant heating rate of 10 K/min. In order to compare the activity of the BaFeO_{3.8} perovskites with reference data from the literature, measurements were also performed using the following, less demanding, experimental conditions described by other authors:^(14, 47) 500 mg of catalysts, total reactant stream flow 100 cm³/min, therefore a spatial velocity much lower, of just 12,000 cm³/h·g. Finally, a feed gas composition with large oxygen excess was used: 1% de CO, 20% de O₂, 79% He.

RESULTS AND DISCUSSION

The chemical composition of the sample, as determined by EDS, TGA and chemical analysis corresponds to Ba(Fe⁴⁺)_{0.56}(Fe³⁺)_{0.44}O_{2.78}. SEM images recorded on the BaFeO_{2.78} sample (Figure S1) show that this material is made up by particles of 150-400 nm. The XRD pattern at room temperature of BaFeO_{2.78} perovskite like-type can be indexed on the basis of a hexagonal unit cell with cell parameters $a=0.5683(1)$, $c=1.4062(1)$ nm and P6₃/mmc (N° 194) space group.^(48,49) No other additional peaks, due to secondary minority phases, are present in the diagrams. Selected Area Electron Diffraction (SAED) along [01-10] and [0001] zone axes confirm the XRD results

(Figure S2). All maxima can be indexed on the basis of the (hcchcc)-6H BaTiO₃ polytype.⁽⁵⁰⁾

Further structural characterization has been performed by NPD at room temperature. The NPD collected for the 6H-phase were fitted with space group P6₃/mmc at room temperature. Fitting of the NPD data and difference profiles between observed and calculated data for 6H are shown in (Figure 1). The refined atomic positions resulting from the refinement are listed in Table S1; Table S2 shows selected interatomic distances. The structure consists of [Fe₂O₉] face-sharing dimers linked by single corner-sharing [FeO₆] units along c-axis (inset in fig.1). There are two crystallographically different octahedral sites in this structure, Fe(1) and Fe(2), which correspond to the isolated corner-sharing octahedron and the face sharing-octahedra dimer, respectively. [Fe(1)O₆] is a very regular site with six identical distances Fe-O (0.2018(4) nm), whereas [Fe(2)O₆] has three short and three long Fe-O distances (see Table S2). The distances obtained from the refinement for Fe octahedrally oxygen coordinated agree well with previous values reported in related phases in the BaFeO_{3.8} system.⁽⁴⁹⁾ As can be observed, to reduce electrostatic repulsions between the metal ions within the face-sharing units, the ions on the Fe(2) sites are displaced from their central positions towards the adjacent cubic layer. Consequently, the face sharing dimers are distorted with three longer and three shorter Fe(2)-O distances. We have refined the occupancy factor of all the oxygen atoms. The obtained occupation numbers reveal almost the same oxygen vacancies in all the cubic and hexagonal layers building the 6H structure. Therefore, they are not preferentially accommodated. The anionic composition of the layers (see Table S1) corresponds to BaO_{2.75(4)} and BaO_{2.78(3)} for cubic and hexagonal layers, respectively. According to this refinement, BaFeO_{2.77(3)} composition per unit formula is obtained in agreement to thermogravimetric data. In the same way, iron presents a 3.54 average oxidation state, in good agreement with that obtained by redox titration analysis.

In order to get more detailed information at atomic level, a STEM and EELS study was performed. Figure 2 shows the atomically resolved HAADF and ABF im-

ages along [01-10] obtained using aberration corrected STEM. Firstly, in the [01-10] HAADF image (Figure 2a) it can be observed an apparently well-ordered material with d_{spacing} of 0.49 and 1.40 nm, corresponding to d_{100} and d_{001} , respectively. The structure can be directly revealed from the contrast observed in the enlarged image at the inset, where the brighter contrast corresponds to the heaviest Ba ($Z = 56$) cations while the Fe ($Z = 26$) columns of atoms are observed as less bright spots. Complementary information about the location of the light elements is provided in the corresponding ABF image (Figure 2b), where atomic columns of oxygen along [010] are clearly resolved. Notice that in the ABF image, the heaviest positions, corresponding to Ba/Fe cations, are seen as the darkest contrast, whereas the oxygen atoms are seen as the less dark contrast. Additionally, the atoms columns distribution from both HAADF and ABF images and the arrangement of hexagonal and cubic layers in the ...cchcch... sequence is in good agreement with the structural model of the 6H-polytype. At this point, it is worth recalling that ABF images in an aberration corrected microscope make it possible to obtain information about the oxygen concentration layer by layer.^(s1) No intensity differences have been detected for the hexagonal and cubic layers in BaFeO_{2.78} meaning, in agreement to NPD results, that there is not a clearly preferential distribution of the oxygen vacancies along the different type of layers.

Detailed information on the chemical composition of this sample with atomic resolution was acquired by combination of STEM and EELS (results are presented in Figure S3). No differences in contrast have been detected in the O mapping meaning similar oxygen content in both h and c layers in agreement to NPD and ABF results.

The thermogravimetric study of the sample has been carried out under H₂/Ar and H₂/He atmospheres in a TGA and electrobalance CAHN D-200, respectively (see Figure S4). From these results, it can be concluded that the reduction process takes place in two defined steps. According to the weight loss, the stoichiometry obtained at the first plateau corresponds to BaFeO_{2.58}, whereas after the second step a final composition close to BaFeO_{2.45} is attained (Figure S4). A further study of the structural features of these

reduced samples has been carried out by XRD and SAED as a function of the temperature. From these results, the 6H-type seems to be stable on the compositional range between $0.22 \leq \delta \leq 0.42$. The XRD pattern of the final product of the TGA experiments shows the presence of a small amount of BaCO₃ indicating that a slight decomposition of the 6H-phase takes place.

A study of the catalyst pretreatment conditions has been performed. To determine the most adequate temperature to clean the surface of the perovskite before running the catalytic activity test, a TPO experiment was ran. Figure S6 shows water and CO₂ evolution as determined from changes in the mass/charge (m/q) ratio 18 and 44 detected during the TPO of BaFeO_{2.78}.

To better understand the oxygen exchange properties of the prepared solids, further characterization of their redox properties was performed through Temperature Programmed Reaction methods under different type of reducing environments: H₂-TPR (figure 3), CO-TPR and He-TPD (Supporting Information figures S7 and S8, respectively). Figure 3 shows the evolution of the most relevant m/q ratios (18 and 32) during the H₂-TPR of BaFeO_{2.78}. The trace of the m/q=18 evolution with temperature shows a broad peak of water evolution centred at about 600 K, suggesting that oxygen from the oxide is being removed as H₂O. Additional reduction events, of lower intensity, are observed at higher temperatures (peaks at 773, 840 and 1020 K). After the latter, a broad and intense reduction event is also observed. The small peak at very low temperature, below 373 K, corresponds to desorption of physically adsorbed water. At this point, it is worth recalling that the catalyst pretreatment method did not guarantee the total elimination of adsorbed water (see S6). It is worth noting that the trace of the m/q=32 evolution with temperature presents a broad maximum centred around 500 K, indicating that, in this temperature range, oxygen comes out of the oxide lattice without combination with hydrogen, but just as O₂. After this peak, O₂ evolution seems also to occur in parallel with H₂O production showing the form of a broader band. From the information provided by these two m/q ratios, it would appear that, in the temperature range of interest for the catalytic process (below 773 K), oxygen leaves the sample in the

presence of hydrogen either as O₂, within the temperature range 423–573 K, and then as H₂O, mostly from 573 up to 723 K. Coming back to the TGA data (Supporting Information S4), the first peak observed in the H₂-TPR curves (close to 500 K) could be associated to the first reduction step giving rise to the BaFeO_{2.58} composition. The second one, around 600 K, should correspond to the second step of the reduction process leading to a final composition close to BaFeO_{2.5}.

Full reduction process has been followed by an electrobalance CAHN D-200 heating the sample up to 900 °C under H₂ atmosphere. The obtained curve is depicted in Figure S5. Besides the two steps previously detected in the TGA experiment, a high number of weight loss steps are also present in agreement with the reduction events previously observed in the H₂-TPR curve (Figure 3). The occurrence of all these reduction events agrees with the high number of weight loss steps observed in the thermogravimetric curve under hydrogen reported in Figure S5, in which at least 6 reduction events are observed. At this point, it is worth recalling that Xian *et al.*⁽⁵²⁾ have reported H₂-TPR results for Ba-Fe perovskites prepared by a sol-gel method and pretreated at 673 K prior to recording the H₂-TPR. In their results, reduction (hydrogen consumption) starts approximately at 690 K, peaking at 773, 923 and 1050 K, in good agreement with our results for the m/q=18 trace. Nevertheless, these authors did not notice the low temperature reduction effects related to O₂ evolution.

Recently, M.M. Natile *et al.*⁽⁵³⁾ have reported an H₂-TPR profile for a ... ccc... stacked LaFeO₃ perovskite. No reduction effect was detected at temperatures below 673 K, being the most important peaks observed at roughly 773 and 1123 K. It is therefore clear that substitution of La by Ba improves significantly the reducibility of the Fe perovskite.

Comparison of the H₂-TPR results with those corresponding to the CO-TPR of the same sample, Figure S7, provides also quite interesting information. Note that in this case, the m/q=32 trace does not show any signal at all, keeping flat in the whole temperature range. Nevertheless, the m/q=44 (CO₂) signal shows a first maximum, around 600 K. Both facts, suggest

that CO is converted to CO₂ by the oxygen species apparent in the low temperature peak of the H₂-TPR. These results provide, therefore, a first evidence of the active role in CO oxidation of this low temperature, labile, lattice oxygen. At this point, it is worth recalling that, the exit of oxygen out of the oxide lattice at low temperature does not require the presence of hydrogen, since it was also detected, within the same temperature range, during He-TPD experiments, Figure S8. It is just, therefore, a thermally driven process.

Oxygen evolution in He-TPD of alkaline-earth substituted LaMO₃ (M=Fe, Co, Mn) perovskites has been reported to occur as two consecutive desorption peaks.^(4,9,13,24,54,55) A broad α peak appears at low temperatures, 573–873 K, followed by a sharp β one at temperatures typically above 973 K. The intensity of the first one has been reported to increase with Sr²⁺ substitution in LaCoO₃^(13,14,17,22–24) and it has been also correlated with the amount of Co⁴⁺ in the perovskite⁽²⁴⁾ and with the catalytic activity in hydrocarbons oxidation.^(56–60) Though very loose and unspecific suggestions are proposed in some of these references, the real fact is that the exact structural origin of these two types of oxygen atoms is far from being clear.

In the BaFeO_{2.78} catalyst prepared here, O₂ evolution takes place mostly within the so-called α peak, which moves down in temperature to just 500 K; this is 100–150 K below the temperature values observed for the α peak maximum in La_xSr_{1-x}CoO₃ perovskites (x=0–0.6).⁽²⁴⁾ This would suggest a good oxidation activity at low temperatures for this BaFeO_{2.78} perovskite (Supporting Information Table S4).

An additional aspect of interest, in connection with the redox behavior of the catalyst and of great importance to sustain a catalytic oxidation cycle, is the reversibility of the lattice oxygen elimination process under an oxidizing atmosphere. To clarify this point, we first studied the reoxidation by TGA, under O₂(5%)/He of BaFeO_{2.78} which was previously reduced under H₂(5%)/Ar at 423 K. As shown in Figure 4 reoxidation was carried out also using a step approach (10 K/min heating rate and 1 h isothermal time). Note that after heating at 373 K, weight gain starts. Raising the temperature up to 473 K increases the oxidation rate. At this temperature, a plateau is

reached at a 1.24% weight gain. The increasing the temperature at 573 K results in a weight loss, this meaning that the labile forms of oxygen leave the sample even under an atmosphere containing 5% O₂. The exit of this oxygen could not be detected in the evolution of the m/q=32 during the TPO experiments because the amount of evolved oxygen results only in a very small change in the oxygen content of the flowing O₂(5%)/He gas stream. These last results indicate that oxygen can reversibly leave and re-enter the oxygen sublattice of BaFeO_{2.78}.

The starting BaFeO_{2.78} sample was also characterized by XPS, Figure S9. Results of the quantitative analysis of the Fe 2p_{3/2}, Ba 3d, O 1s and C 1s peaks, included in Table S4, point out to a Ba/Fe ratio at the surface close to the nominal. The O/(Ba+Fe) ratio of 3.2 evidences the formation of carbonates on the Ba centres at the surface, as it is confirmed by the presence of two differentiated peaks in the Ba 3d_{5/2} signal; one at 779.8 eV, which can be assigned to BaCO₃, and a second one at 778.7 eV due to Ba bonded to O (BaO). Deconvolution of this signal indicates an 86% contribution of the carbonate form. The O 1s and C 1s signals do also evidence the presence of carbonates at the surface. These surface carbonates must be related to exposure to air after the preparation, since no secondary phase was found by XRD.

Concerning the oxidation state of Fe at the surface of the starting oxide, the analysis of the Fe 2p_{3/2} signal points out to a 100% Fe³⁺, although the overall oxygen content of the sample, determined by EELS and TGA, is BaFe^{+3.56}O_{2.78}. According to the TPD results, the BaFeO_{2.78} perovskite loses oxygen at intermediate and high temperatures.

Putting together XPS and EELS data, it seems that the starting, as synthesized, oxide is made up of crystallites whose bulk is Fe⁴⁺ rich and with a surface mostly made of Fe³⁺ species. Nevertheless, it is important to recall, as described in the experimental section, that prior to both chemical and catalytic essays, the oxide was submitted to a cleaning treatment under oxidizing atmosphere, 5% O₂/He, at low temperature, 523 K, which, according to TGA experiments, allows its reoxidation. Therefore, the actual state of the surface of the oxide before catalytic measurements must

correspond to an oxidation state close to the bulk. However, this temperature is not high enough to eliminate carbonates; so Ba species at the surface after the cleaning step must be carbonated.

In order to compare with other iron based perovskites, the activity of BaFeO_{2.78} was measured. The comparison of the light-off curves (catalytic activity vs reaction temperature) for CO oxidation of BaFeO_{2.78} with those based on lanthanides indicate that the Ba perovskite is more active than the latter in the whole temperature range. Table S4 gathers the characteristic temperature values at which CO conversion reaches 50% ($T_{50\%}$). The values reported for BaFeO_{2.78} are between 50 and 80 K below those of the lanthanide based perovskites, NdFeO₃ being the closest one. Therefore, substitution of any of these lanthanides by Ba results in a clear improvement of catalytic activity in CO oxidation in the whole temperature range. As shown in last column of Table S4, the BET surface areas of the different perovskites are similar, this making the comparison meaningful. In any case, as can be seen from the Table S4, for both LaFeO₃ perovskites, increasing the surface area around these values only changes the results observed at the lowest reaction temperatures, *i.e.*, in the limit of low CO conversions. Regarding other alkaline-earth iron related perovskites, only catalytic activity has been reported for the oxygen reduced SrFeO_{3-δ} system,⁽⁶¹⁾ since in the Ca-Fe-O one, pO₂ > 20 kb is needed to stabilize Fe(IV) as CaFeO₃.^(62, 63) SrFeO_{3-δ} materials show complex perovskite related superstructures in which part of the Fe cations are five-fold coordinated in a pyramidal configuration. Although, as far as we know, no data are currently reported concerning the CO oxidation activity of (Ca, Sr)-Fe perovskites, SrFeO_{3-δ} materials have been tested as catalysts for methane oxidation⁽⁶¹⁾ or even, for toluene combustion.⁽⁶⁴⁾

The influence of redox pretreatment on the catalytic behavior of BaFeO_{2.78} was also studied. For this purpose, the activity of two additional samples was measured: (1) that obtained after reducing the initial BaFeO_{2.78} catalysts under H₂(5%)/Ar at 523 K and (2) that obtained after reduction at 623 K. In Figure 5, the light-off curves of these two samples are compared with that of fresh BaFeO_{2.78}. Note how after reduction

at 523 K a significant shift towards higher temperatures takes place in the whole temperature range. Increasing the reduction temperature up to 623 K gives rise to a further upwards displacement in the temperature scale, though the effect in this case is much less pronounced. In terms of light-off temperature values (Table 1), the transformation of BaFeO_{2.78} into BaFeO_{2.58} results in a 46 K increase, whereas only a further 15 K increase is observed for the reduction at 623 K. These results suggest that the labile oxygen types present in the most oxidized perovskite are very active towards CO oxidation, in good agreement with the results observed in the CO-TPR experiments. Elimination of this oxygen by the reduction treatment leads to a solid with less catalytic activity, this pointing out to a likely involvement of these oxygen species into the reaction mechanism. In other words, there is a direct correlation between catalytic activity and the oxygen content, *i.e.*, the Fe⁴⁺ concentration in the perovskite.

These results contrast apparently with others reported in papers in which a specific analysis of such correlation is studied, as it is the case of those reported by Fierro *et al*⁽⁶⁵⁾ for the CO oxidation behavior of oxygen-deficient LaCuO_{3-δ} perovskites ($0.05 \leq \delta \leq 0.45$). These authors concluded explicitly on a direct correlation between the total oxygen vacancies content of this type of perovskites (δ) and the catalytic activity. Nevertheless, a more detailed consideration of their conclusions reveal that they finally propose that the highest activity observed for the catalyst with the highest concentration of vacancies, LaCuO_{2.55} ($\delta=0.45$) was due to the formation of a surface, nanometer-thick, layer of a Cu³⁺ rich perovskite; *i.e.*, of a nearly fully oxidized (very low δ) surface. In essence, they make a difference between total vacancy content (total or bulk δ) and surface vacancies content (surface δ). In this framework, their results totally agree with those obtained by us on the BaFeO_{3-δ} perovskites. Zhang *et al*⁽⁶⁶⁾ recently concluded similar results from a detailed analysis of oxygen exchange properties, including isotopic exchange reactions and catalytic behavior in CO oxidation, on LaFe_{1-x-y}Cu_xPd_yO_{3-δ}. As proposed here, availability of low temperature oxygen species, in that case promoted by an increase in oxygen mobility in the oxide, is pointed out as the origin of a

higher CO oxidation activity.

In order to investigate the effect of the temperature and atmosphere on the BaFeO_{2.78}, a detailed structural study of this catalyst has been carried out by means of *in situ* high-temperature XRD (HT-XRD) and SAED (HT-SAED) reproducing the catalyst pre-treatment conditions. The *in-situ* HT-XRD study was carried out at $20 \leq 2\theta \leq 80^\circ$ and the most interesting 2θ range ($22-32^\circ$) is plotted in Figure 6. The experiment consisted in increasing the sample temperature in vacuum from RT (indicated by RT-1 in Figure 6) up to 673 K. A diffractogram was taken of the sample after increasing the temperature each 100 K, maintained for 30 min. Subsequently, once a temperature of 673 K was reached, a cooling down process to RT in oxygen atmosphere was carried out (indicated by RT-2 in Figure 6). The peaks are represented by two different colours: the green colour is attributed to the XRD patterns acquired under vacuum and the orange ones correspond to the patterns under oxygen atmosphere.

The principal peaks can be indexed on the basis of the hexagonal 6H structure characteristic of the starting BaFeO_{2.78} phase. With increasing the temperature from 298 up to 673 K, the peaks intensities for BaFeO_{3-δ} decrease and a small peak, which takes the form of a broad appear on the left side of all the 6H reflections. These features are clearly observed in the pattern corresponding to 673 K (Figure 6). These extra reflections quickly disappear in the first steps of the cooling process under oxygen atmosphere. Furthermore, all reflections recover their initial intensities and the appearance of RT1 pattern is totally recovered (Figure 6).

These results help us building up structural ideas about the redox behavior of BaFeO_{2.78} under vacuum and oxidizing atmospheres. In fact, the splitting of all the 6H reflections point to the formation of a secondary 6H phase with higher values of cell parameters and therefore with a lower oxygen content. The possibility that such features could be associated to the presence of a structural distortion of the ideal 6H polytype due to an ordered distribution of the oxygen vacancies throughout the structure cannot be initially ruled out. The Rietveld refinement of the XRD data taken at 673

K under vacuum allows us to reject definitely this possibility (Figure S10). Actually, the whole diffraction pattern is well fitted to two 6H phases with different unit cell metrics; a majority phase with $a=0.57526(3)$ and $c=1.39927(5)$ nm and a minority one with $a=0.58111(5)$ and $c=1.4002(2)$ nm. This result rules out an orthorhombic distortion of the 6H polytype.

At this point, it is worth recalling that the reduction process in bulk $\text{BaFeO}_{3-\delta}$ takes place at high temperatures (>1000 °C). Under these conditions, such reduction process is accompanied by the formation of cubic oxygen deficient BaO_{3-x} layers that break the (cchccch)-6H sequence giving rise to highly disordered hexagonal structures up to around $\delta = 0.45^{(36)}$, where cubic phases are stabilized. The reduction process of the studied nano $\text{BaFeO}_{2.78}$ sample occurs under soft conditions ($T \approx 200$ °C). The easy reversibility of the reduction process under these conditions, suggest a different reduction pathway. To get more information about the evolution of the crystal structure in the sample with nanosized crystallites, we have undertaken a study by transmission electron microscopy using a heating stage. These experiments were designed to characterize the reciprocal lattice at room temperature, 523 and 623 K.

Due to the high vacuum inside the column of the electron microscope, along with the high temperature and the energy of the incident beam of electrons, a quite reductive atmosphere should be present, which should mimic the conditions of a reduction process and push the perovskite to desorb oxygen. The step one of these experiments was to select several crystals to reach the major zone axes SAED patterns, [1-10] and [001], at room temperature. At this step, we just found crystals showing the associated reciprocal lattices corresponding to the 6H starting phase (Fig. 7a and 7b). The patterns shown in Figure 7c and d were recorded after some minutes at 523 K. It can be seen that the SAED patterns transform at this temperature, with additional satellites reflections appearing along [1-10] and equivalent directions (Fig. 7c and 7d). All satellite reflections in (c) could be indexed by assuming a modulation wave vector of the type $q_1=1/3[10-10]^*$. Looking now to the perpendicular reciprocal

plane shown in (d), [0001], the needed wave vector to index all satellite reflections is of the type $q_3=1/7[21-30]^*$. Finally, after heating up the stage at 623 K, new satellites reflections, always along [110] and equivalent directions are observed (Fig. 7e and f). In Figure 7f down <01-10>, satellites are of the type q_1 . It is worth recalling that in all cases the reflections appear in the *ab* plane, *i.e.*, in the BaO_3 layers. In any crystal extra spots along c^* are observed. Finally, we did cool down to room temperature; we did put away the sample holder from the microscope and wait for some minutes to insert it back into the column of the microscope. The electron diffraction patterns are as the ones observed at room temperature in the starting material (fig. 7a and b). These results show that, in this case, the oxygen vacancies are accommodated over the different BaO_{3-x} layers without any modification in their stacking sequence, thus, keeping the basic structure of the 6H type. This allows an easy and reversible reduction/oxidation process that should be related to the catalyst behavior of the studied phase.

To propose a mechanism for the catalytic behavior of $\text{BaFeO}_{3-\delta}$ is essential to know the nature of the active sites. Although, in general, it is accepted that the active sites involve both oxygen vacancies and metal cation occupying the position B of the ABO_3 perovskite, ($--\square-\text{B}^{n+}-\square-$), the actual structure of these sites remains unknown.

To identify the elements that form the active sites, Teraoka *et al*⁽⁶⁷⁾ and Shin *et al*⁽⁶⁸⁾ studied the decomposition reactions of nitrogen oxide (NO), in which the oxygen lattice comes into play, finding that the active site is composed of two B cations and two adjacent oxygen vacancies ($\square-\text{B}^{n+}-\square-\text{B}^{n+}$). Additionally, studies of catalytic activity of the material $\text{LaSrNi}_{1-x}\text{Al}_x\text{O}_4$ and $\text{La}_{2-x}\text{Sr}_x\text{CuO}_4$ in the NO decomposition reaction revealed that the structure with an oxygen network situated between two B cations and two oxygen vacancies linked to the B cation ($\square-\text{B}^{n+}-\text{O}-\text{B}^{n+}-\square$) is more favorable for the reaction, further suggesting the importance of oxygen in the crystal lattice of the active site.⁽⁶⁹⁾ In this point, it is worth mentioning that two mechanisms, as a function of the temperature, have been proposed for the catalytic action of perovskites. On the one hand, at low temperatures, a mechanism

has been described in which only surface species are involved in the oxidation process (suprafacial mechanism). CO oxidation has been associated to proceed through this mechanism. On the other hand, at higher temperature, an intrafacial mechanism, similar to the Mars and Van Krevelen mechanism, is proposed.⁽⁷⁰⁾ Steps of the suprafacial mechanism remain valid, but the oxygen anions can migrate from the bulk to the surface to fill in the oxygen vacancies so that, virtually, all oxygens of the bulk can participate in the oxidation process.

The whole set of experimental results presented up to this point suggest a mechanism of CO oxidation on BaFeO_{2.78} catalyst involving the participation of both the perovskite oxygen lattice and the anionic vacancies generated during the conversion process.

The mechanism would include the following steps: the CO conversion on the perovskite BaFeO_{3-δ} starts with the diffusion of the CO_(g) molecules to the perovskite surface. CO molecules are adsorbed on the active sites, CO_(s). The active sites involved in this process would be located in the oxygen vacant sites in deficient [FeO_{6-δ}] octahedra. Once the CO_(s) molecule is adsorbed, the oxygen sublattice perovskite transfers oxygen to it, leading to an oxidized, adsorbed, CO₂ molecule, i.e., CO_{2(s)}, whereas new vacancies in the anionic sublattice perovskite are generated. Then, the CO_{2(s)} molecule desorbs into the gas phase from the perovskite surface and simultaneously the oxygen molecule O_{2(g)}, present in the reaction environment, interacts with the anionic vacancy position, causing the sublattice oxygen regeneration previously lost during the CO_{2(g)} formation process. This last step in this mechanism consists in the surface oxygen atoms diffusion towards the perovskite to refill the anionic vacancies present in the bulk, this reoxidizing the catalyst to its initial state. After this reoxidation step, the catalyst surface becomes ready to start another CO conversion cycle.

CONCLUSIONS

An oxygen-deficient BaFeO_{3-δ} perovskite prepared by a sol-gel route has been characterized from the structural and catalytic points of view. The structure of both the cation and oxygen sublattices has been revealed by a unique combination of XRD, NPD and several advanced STEM techniques, including some *in-situ* type studies evidencing a complex 6H-BaTiO₃ polytype structure, with oxygen vacancies randomly distributed over the hexagonal and cubic layers of the polytype and Fe atoms in a 3.56 average oxidation state.

Redox study evidences the evolution of a labile fraction of oxygen, which allows for a reversible reduction/oxidation, according to *in-situ* XRD and SAED experiments. The oxygen evolution makes that the catalytic activity in CO oxidation of the perovskite is sensitive to the exact activation pretreatment used to clean its surface, a question which has not received the necessary attention in the existing literature. BaFeO_{2.78} depicts a CO oxidation activity superior to that previously reported for other lanthanides-iron perovskites. This highlights the potential of this oxide as noble-metal and lanthanide free catalyst for this process.

Data on the different oxidation states point out to an intra-facial type mechanism for CO oxidation on this perovskite, which contrasts with previous proposal made for this reaction on other perovskites. The large lability detected for a fraction of the oxygen and the accommodation of non-stoichiometry preserving the hexagonal 6H structure seem to be at the roots of this particular behavior.

Quite important, yet insufficiently realized up to now, advanced STEM techniques appear as irreplaceable tools to establish reliable correlations between the defect structure and chemical functionality of perovskite based materials, particularly in the field of heterogeneous catalysis. In this application field, macroscopic, averaging characterization tools, though completely necessary, reveal nevertheless as limited to adequately picture atomic scale details of the active sites.

ASSOCIATED CONTENT

Supporting Information. Experimental details including Chemical analysis, Microstructural characterization, Powder Neutron Diffraction, Thermogravimetric analysis, Study of catalyst pre-treatment conditions,

Study of catalyst conditions, XPS analysis and Rietveld refinement of the XRD under vacuum conditions. The Supporting Information is available free of charge on the ACS Publications website.

AUTHOR INFORMATION

Corresponding Authors

* e-mail: jgcalbet@ucm.es, Tfno: +34 91 394 41 88, Fax: +34 91 394 43 52

Author Contributions

The manuscript was written through contributions of all authors. All authors have given approval to the final version of the manuscript.

ACKNOWLEDGMENT

We thank Dr. J. García-García for his technical support in the microscopy experiments and his help in the scientific discussion of this paper. Dr. E. Matesanz is acknowledged for XRD facilities. We also thank Dr. M. T. Fernández-Díaz for assistance in collecting the neutron powder diffraction data and the Institute Laue Langevin for facilities. Financial support from MINECO (Spain) through Research Projects MAT2014-54372-R, MAT2013-40823-R and CSD2009-00013 are gratefully acknowledged. J.C.H.-G. acknowledges support from the Ramón y Cajal Fellowships Program of MINECO (RYC-2012-10004).

REFERENCES

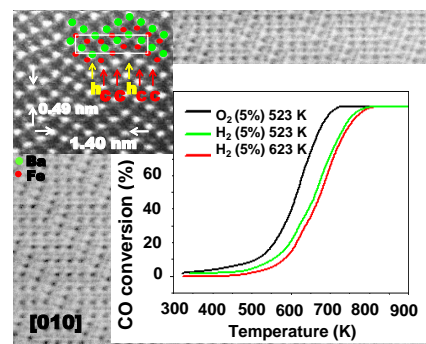
- (1) Critical Raw Materials for the EU, Ad-hoc Working Group on defining critical raw materials of the European Commission; **2010**.
- (2) U. S. Department of Energy in Critical Materials Strategy. **2010**.
- (3) Humphries, M. in Rare Earth Elements: The Global Supply Chain, **2012**.
- (4) Royer, S.; Duprez, D.; Can, F.; Courtois, X.; Batiot-Dupeyrat, C.; Laassiri, S.; Alamdar, H. *Chem. Rev.* **2014**, *114*, 10292-10368.
- (5) Peña, M. A.; Fierro, J. L. G., *Chem. Rev.* **2001**, *101*, 1981-2017.
- (6) Spinicci, R.; Tofanari, A.; Faticanti, M.; Pettiti, I.; Porta, P. *J. Mol. Catal. A-Chem.* **2001**, *176*, 247-252.
- (7) Yang, M.; Xu, A.; Du, H.; Sun, C.; Li, C. *J. Hazard. Mater.* **2007**, *139*, 86-92.
- (8) Villoria, J. A.; Mota, N.; Al-Sayari, S. A.; Álvarez-Galván, M. C.; Navarro, R. M.; Fierro, J. L. G., *Micro and Nanosystems* **2012**, *4*, 231-252.
- (9) Zhu, J.; Li, H.; Zhong, L.; Xiao, P.; Xu, X.; Yang, X.; Zhao, Z.; Li, J. *ACS Catal.* **2014**, *4*, 2917-2940.
- (10) Xu, W.; Cai, J.; Zhou, J.; Ou, Y.; Long, W.; You, Z.; Luo, Y. *Chem-CatChem* **2016**, *8*, 417-425.
- (11) Zhang, R.; Li, P.; Xiao, R.; Liu, N.; Chen, B. *Appl. Catal. B-Environ.* **2016**, *196*, 142-154.
- (12) Libby, W. F. *Science* **1971**, *171*, 499-500.
- (13) Tabata, K.; Misono, M. *Catal. Today* **1990**, *8*, 249-261.
- (14) Ciambelli, P.; Cimino, S.; De Rossi, S.; Lisi, L.; Minelli, G.; Porta, P.; Russo, G. *Appl. Catal. B-Environ.* **2001**, *29*, 239-250.
- (15) Seyfi, B.; Baghalha, M.; Kazemian, H. *Chem. Eng. J.* **2009**, *148*, 306-311.
- (16) Yang, W.; Zhang, R.; Chen, B.; Bion, N.; Duperz, D.; Royer, S. J. *Catal* **2012**, *295*, 45-58.
- (17) Patel, F.; Patel, S. *Procedia Engineering* **2013**, *51*, 324-329.
- (18) Ivanov, D. V.; Pinaeva, L. G.; Isupova, L. A.; Sadovskaya, E. M.; Prosvirin, I. P.; Gerasimov, E. Y.; Yakovleva, I. S. *Appl. Catal. A* **2013**, *457*, 42-51.
- (19) Dong, F.; Chen, Y.; Chen, D.; Shao, Z. *ACS Appl. Mater. Interfaces* **2014**, *6*, 11180-11189.
- (20) Huang, C.; Zhu, Y.; Wang, X.; Liu, X.; Wang, J.; Zhang, T. *J. Catal.* **2017**, *347*, 9-20.
- (21) Li, X.; Yan, X.; Zuo, S.; Lu, X.; Luo, S.; Li, Z.; Yao, C.; Ni, C.; *Chem. Eng. J.* **2017**, *320*, 211-221.
- (22) Taguchi, H.; Yamasaki, S.; Itadani, A.; Yosinaga, M.; Hirota, K. *Catal. Commun.* **2008**, *9*, 1913-1915.
- (23) Saracco, G.; Scibilia, G.; Iannibello, A.; Baldi, G. *Appl. Catal. B-Environ.* **1996**, *8*, 229-244.
- (24) Yamazoe, N.; Teraoka, Y. *Catal. Today* **1990**, *8*, 175-199.
- (25) Grimaud, A.; May, K. J.; Carlton, C. E.; Lee, Y.-L.; Risch, M.; Hong, W. T.; Zhou, J. *Nature Comm.* **2013**, *4*:2439, 1-7
- (26) Ma, A. J.; Wang, S.-Z.; Liu, C.; Xian, H.; Ding, Q.; Guo, L.; Meng, M.; Tan, Y.-S.; Tsubaki, N.; Zhang, J.; Zheng, L.-R.; Li, X. -G. *Appl. Catal. B-Environ.* **2014**, *146*, 24-34.
- (27) Gholizadeh, A. *J. Am. Ceram. Soc.* **2017**, *100*, 859-866.
- (28) Fujishiro, F.; Fukasawa, K.; Hashimoto, T. *J. Am. Ceram. Soc.* **2011**, *94*, 3675-3678.
- (29) Fujishiro, F.; Kojima, Y.; Hashimoto, T. *J. Am. Ceram. Soc.* **2012**, *95*, 3634-3637.
- (30) Ge, C.; Li, L.; Xian, H.; Yan, H.; Meng, M.; Li, X. *Fuel Proc. Technol.* **2014**, *120*, 1-7.
- (31) Xian, H.; Zhang, X.; Li, X.; Li, L.; Zou, H.; Meng, M.; Li, Q.; Tan, Y.; Tsubaki, N. *J. Phys. Chem. C* **2010**, *114*, 11844-11852.
- (32) Li, X.; Chen, J.; Lin, P.; Meng, M.; Fu, Y.; Tu, J.; Li, Q. *Catal. Commun.* **2004**, *5*, 25-28.
- (33) González-Calbet, J. M.; Parras, M.; Vallet-Regí, M.; Grenier, J. C. *J. Solid State Chem.* **1990**, *86*, 149-159.
- (34) Huang, Y.-L.; Pellegrinelli, C.; Wachsman, D. *ACS Catal.* **2016**, *6*, 6025-6032.
- (35) Hayashi, N.; Yamamoto, T.; Kageyama, H.; Nishi, M.; Watanabe, Y.; Kawakami, T.; Matsushita, Y.; Fujimori, A.; Takano, M. *Angew. Chem. Int. Edit.* **2011**, *50*, 12547-12550.
- (36) Carbonio, R. E.; Fierro, C.; Tryk, D.; Scherson, D.; Yeager, E. J., *J. Power Sources* **1988**, *22*, 387-398.
- (37) Falcon, H.; Carbonio, R. E., *J. Electroanal. Chem.* **1992**, *69*, 339-344.
- (38) Falcon, H.; Goeta, A. E.; Punte, G., *J. Solid State Chem.* **1997**, *133*, 379-385.
- (39) Yamada, I.; Tsuchida, K.; Ohgushi, K.; Hayashi, N.; Kim, J.; Tsuji, N.; Takahashi, R.; Matsushita, M.; Nishiyama, N.; Inoue, T.; Irifuné, T.; Kato, K.; Takata, M.; Takano, M. *Angew. Chem. Int. Edit.* **2011**, *50*, 6579-6582.
- (40) Falcón, H.; Martínez-Lope, M. J.; Alonso, J. A.; Fierro, J. L. G. *Appl. Catal. B-Environ.* **2000**, *26*, 131-142.
- (41) Pennycook, S. J.; Nellist, P. D., Eds. in Scanning Transmission Electron Microscopy: Imaging and Analysis. Elsevier: **2011**.
- (42) Tendeloo, G. V.; Dyck, D. V.; Pennycook, S. J. Eds. in Handbook of Nanoscopy, Wiley-VCH **2012**.
- (43) Rodríguez-Carvajal, J. *Phys. B* **1993**, *192*, 55-69

- (44) Bonnet, N.; Brun, N.; Colliex, C. *Ultramicroscopy* **1999**, 77, 97.
(45) <http://hyperspy.org>; DOI 10.5281/zenodo.16850.
(46) Egerton R. F, in Electron energy-loss spectroscopy in the electron microscope, Plenum, New York, **1996**.
(47) Colonna, S.; De Rossi, S.; Faticanti, M.; Pettiti, I.; Porta P. *J. Mol. Catal. A: Chem.* **2002**, 187, 269-276.
(48) Jacobson, A. J.; *Acta Cryst. B32*, **1976**, 1087-1090.
(49) Parras, M.; Vallet-Regi, M.; Gonzalez-Calbet, J. M.; Grenier, J. C. *J. Solid State Chem.* **1989**, 83, 121-131.
(50) Burbank, R. D.; Evans, H. T. *Acta Crystallogr.* **1948**, 1, 330-336.
(51) Kobayashi, S.; Findlay, S. D.; Shibata, N.; Mizoguchi, T.; Sato, Y.; Okunishi, E.; Ikuhara, Y.; Yamamoto T. *Appl. Phys. Lett.* **2012**, 100, 193112-5.
(52) Xian, H.; Li, F. L.; Li, X. G.; Zhang, X. W.; Meng, M.; Zhang, T. Y.; Tsubaki, N. *Fuel Process. Technol.* **2011**, 92, 1718-1724.
(53) Natile, M. M.; Ponzoni, A.; Concina, I.; Glisenti, A. *Chem. Mater.* **2014**, 26, 1505-1513
(54) Gunasekaran, N.; Rajadurai, S.; Carberry, J. J.; Bakshi, N.; Alcock, C.B. *Solid State Ionics* **1994**, 73, 289-295.
(55) Gunasekaran, N.; Rajadurai, S.; Carberry, J. J.; Bakshi, N.; Alcock, C.B.; *Solid State Ionics* **1995**, 81, 243-249.
(56) Nakamura, T.; Misono, M.; Yoneda, Y., *Chem. Lett.* **1981**, 1589-1592.
(57) Nakamura, T.; Misono, M.; Yoneda, Y., *J. Catal.* **1983**, 83, 151-159.
(58) Teraoka, Y.; Furukawa, S.; Yamazoe, N.; Seiyama, T., *Nippon Kagaku Kaishi* **1985**, 1529-1534.
(59) Seiyama, T.; Yamazoe, N.; Eguchi, K., *Ind. Eng. Chem. Prod. Res. Dev.* **1985**, 24, 19-27.
(60) Nakamura, T.; Misono, M.; Yoneda, Y., *Bull. Chem. Soc. Jpn.* **1982**, 55, 394-399.
(61) Falcon, H.; Barbero, J. A.; Alonso, J. A.; Martínez-Lope, M. J.; Fierro, J. L. G. *Chem. Mater.* **2002**, 14, 2325-2333.
(62) Takeda, Y.; Naka, S.; Takano, M. *J. Physique*, **1979**, 40, 331-332.
(63) Woodward, P. M.; Cox, D. E.; Moshopoulou, E.; Sleight, A. W.; Morimoto, S. *Phys. Rev. B* **2000**, 62, 844-855.
(64) Ji, K.; Dai, H.; Dai, J.; Deng, J.; Wang, F.; Zhang, H.; Zhang, L. *Catal. Today* **2013**, 201, 40-48.
(65) Falcon, H.; Martinez-Lope, M. J.; Alonso, J. A.; Fierro, J. L. G. *Appl. Catal. B: Environmental* **2000**, 26, 131-142.
(66) Zhang, R.; Chen, B.; Bion, N.; Duprez, D.; Royer, S. *J. Catal.* **2012**, 295, 45-58.
(67) Teraoka, Y.; Harada, T.; Kagawa, S. *J. Chem. Soc. Faraday Trans.* **1998**, 94, 1887-1891.
(68) Shin, S.; Arakawa, H.; Hatakeyama, Y.; Ogawa, K.; Shimomura, K. *Mater. Res. Bull.* **1979**, 14, 633-639.
(69) Zhu, J.; Yang, X.; Xu, X.; Wei, K. *J. Phys. Chem. C*, **2007**, 111, 1487-1490.
(70) Doornkamp, C.; Ponec, V. *J. Mol. Catal. A: Chemical*, **2000**, 162, 19-32.

1
2
3
4
5 Achraf el Hadri, Isabel Gómez-Recio, Eloy del
6 Río, Juan C. Hernández-Garrido, Raquel Cortés-Gil,
7 María Hernando, Aurea Varela, Angel Gutiérrez,
8 Marina Parras, Juan J. Delgado, José A. Pérez-Omil,
9 Ginesa Blanco, José J. Calvino, José M. González-Calbet

10
11 ACS Catal. 2017
12
13

14 Critical Influence of Redox Pretreatments
15 on the CO Oxidation Activity of $\text{BaFeO}_{3-\delta}$
16 Perovskites: An In-Depth Atomic Scale
17 Analysis by Aberration-Corrected and *In-Situ*
18 Diffraction Techniques



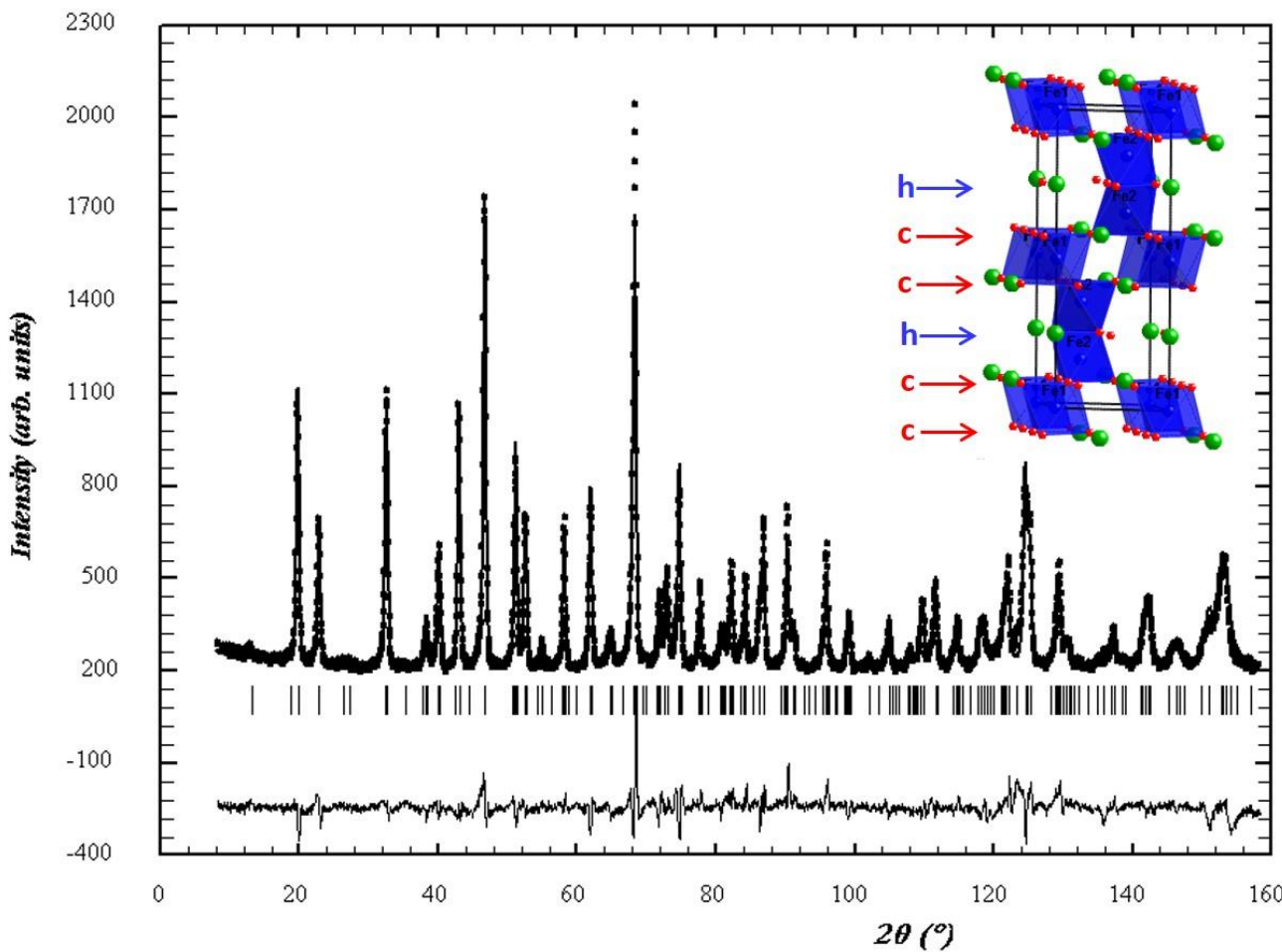


Figure 1. Observed, calculated, and difference profile of NPD patterns for BaFeO_{2.78} at room temperature. Inset: Structural model for 6H-BaFeO_{2.78}.

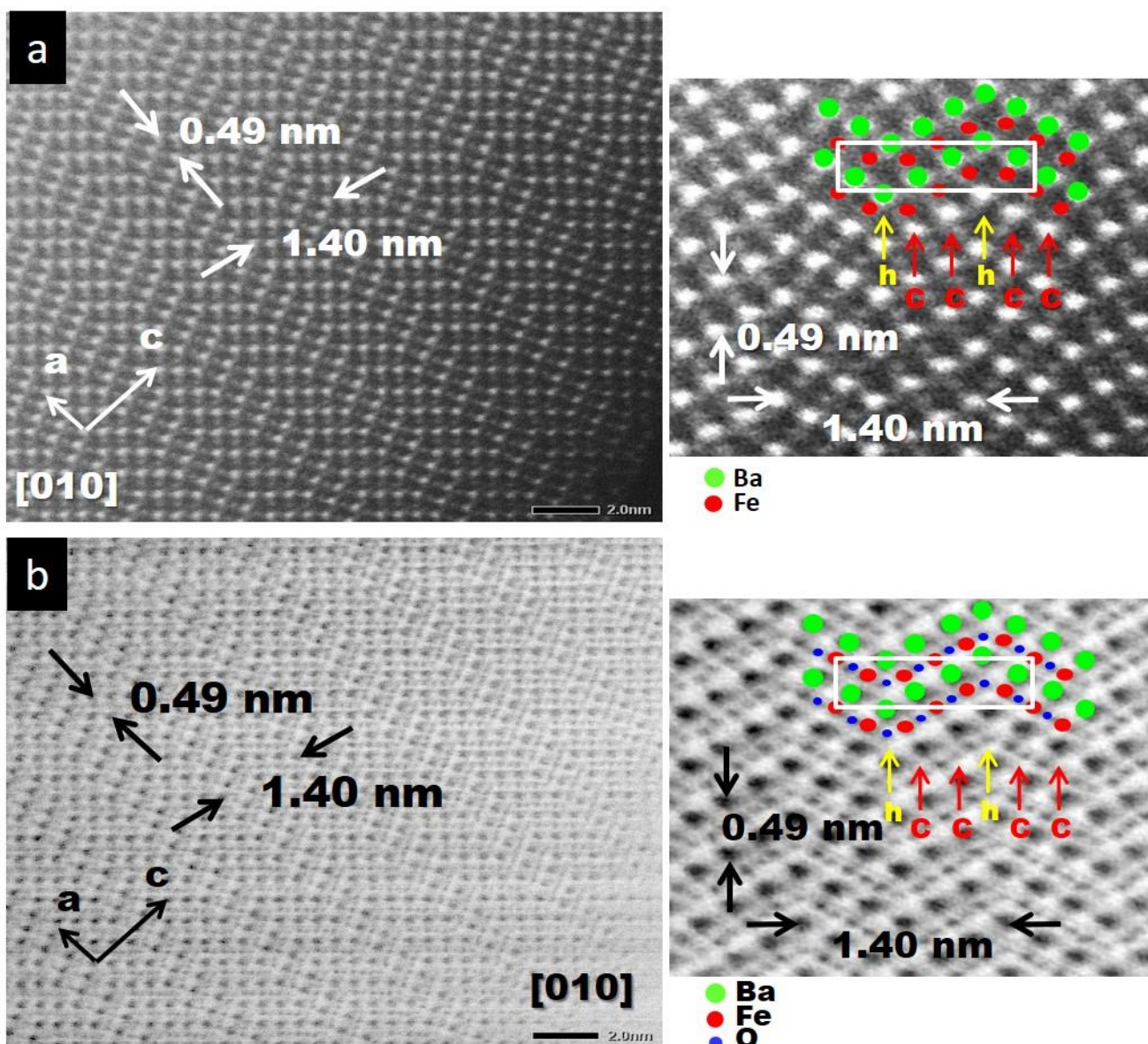


Figure 2: a) Atomically resolved HAADF and b) ABF images along [010] zone axis of 6H-BaFeO_{2.78}. Insets show the respective enlarged images in which the schematic atomic model is included.

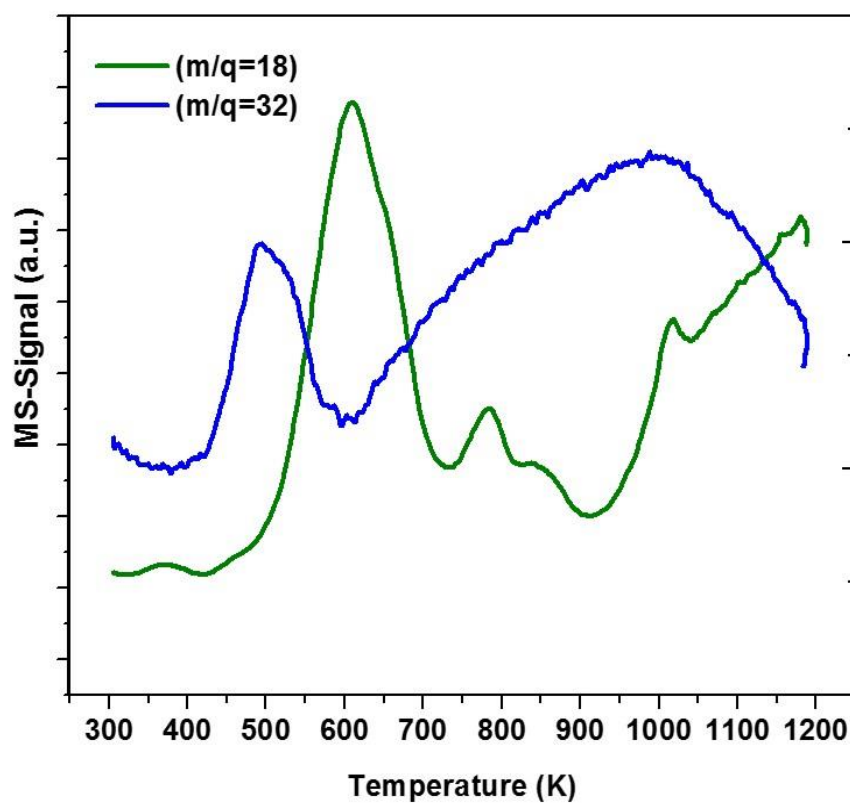


Figure 3. H₂-TPR measurements under flowing H₂ (5%)/Ar study for BaFeO_{2.78}.

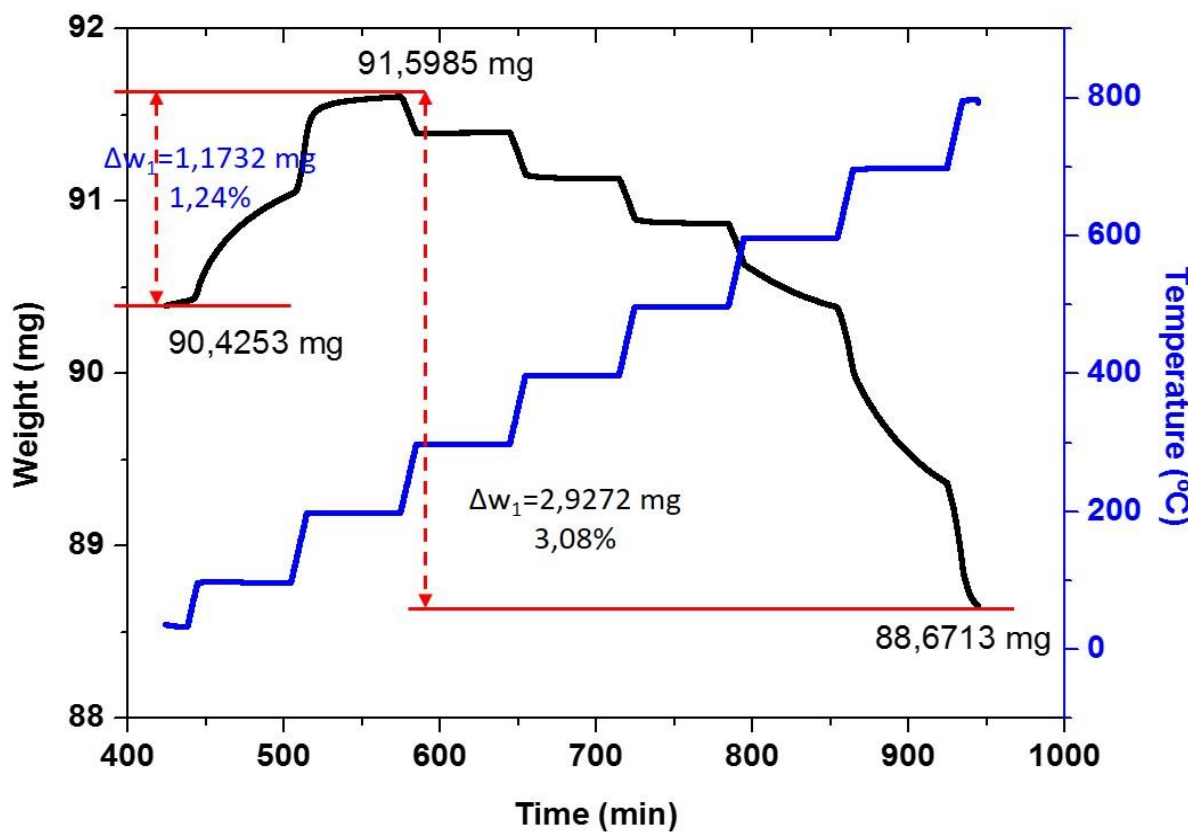


Figure 4. Weight modifications during the heating under O_2/He of a sample 6H- $\text{BaFeO}_{2.78}$ catalysts previously reduced in $\text{H}_2(5\%)/\text{Ar}$.

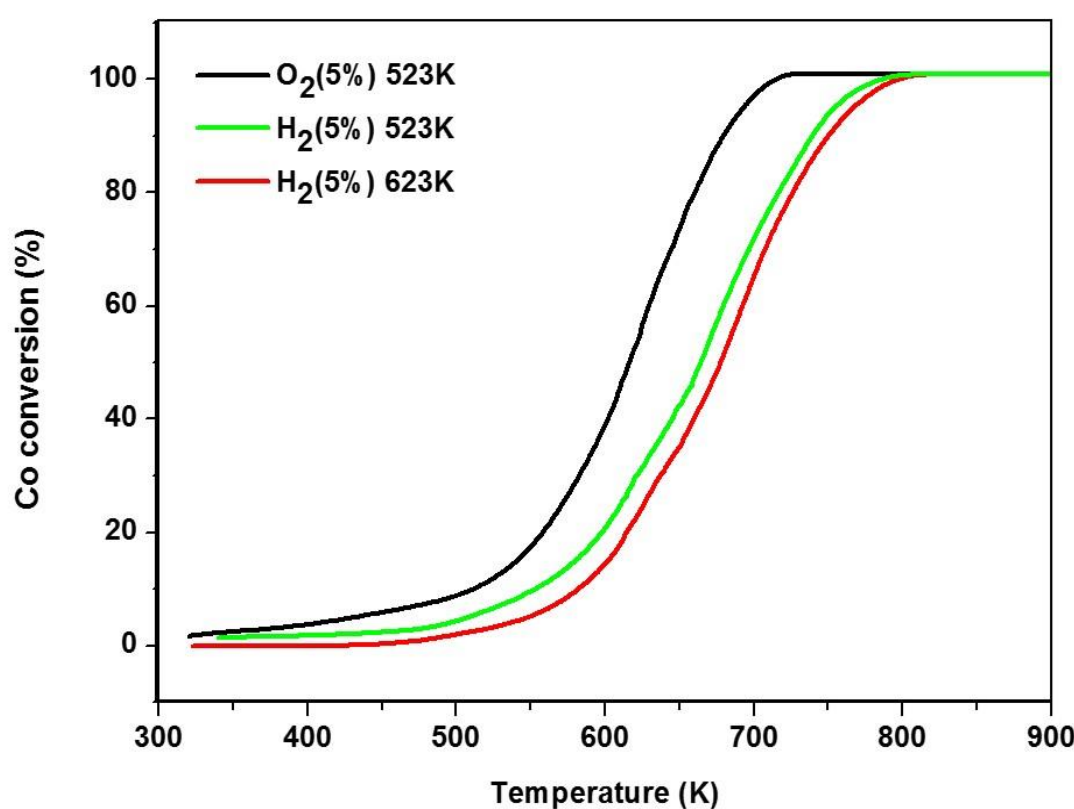


Figure 5. Catalytic oxidation of CO. Comparison of light off curves corresponding to the fresh 6H-BaFeO_{2.78} (black) and 6H-BaFeO_{2.78} pretreated at 523 (green) and 623 K (red) in 5% H₂/Ar.

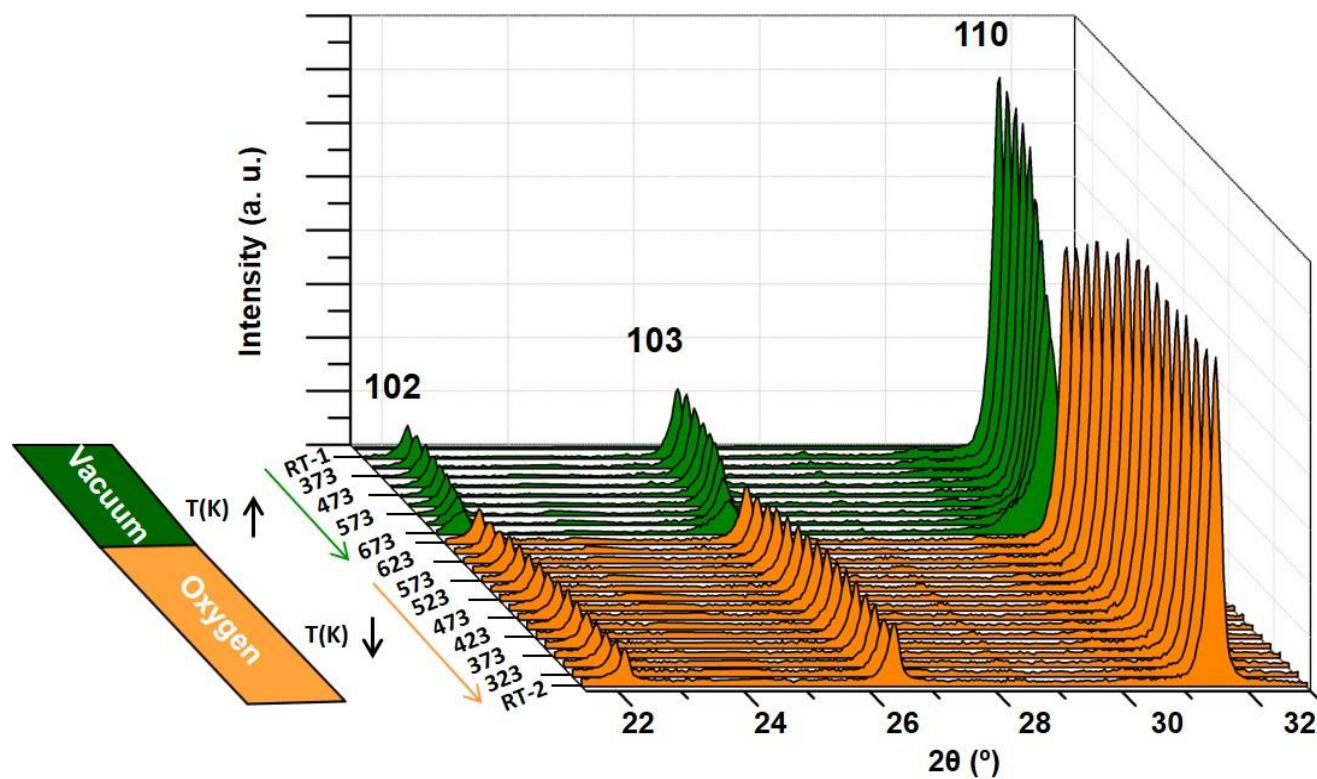


Figure 6. Thermal evolution of the XRD patterns collected *in situ* in vacuum (green color) and oxygen atmosphere (orange color).

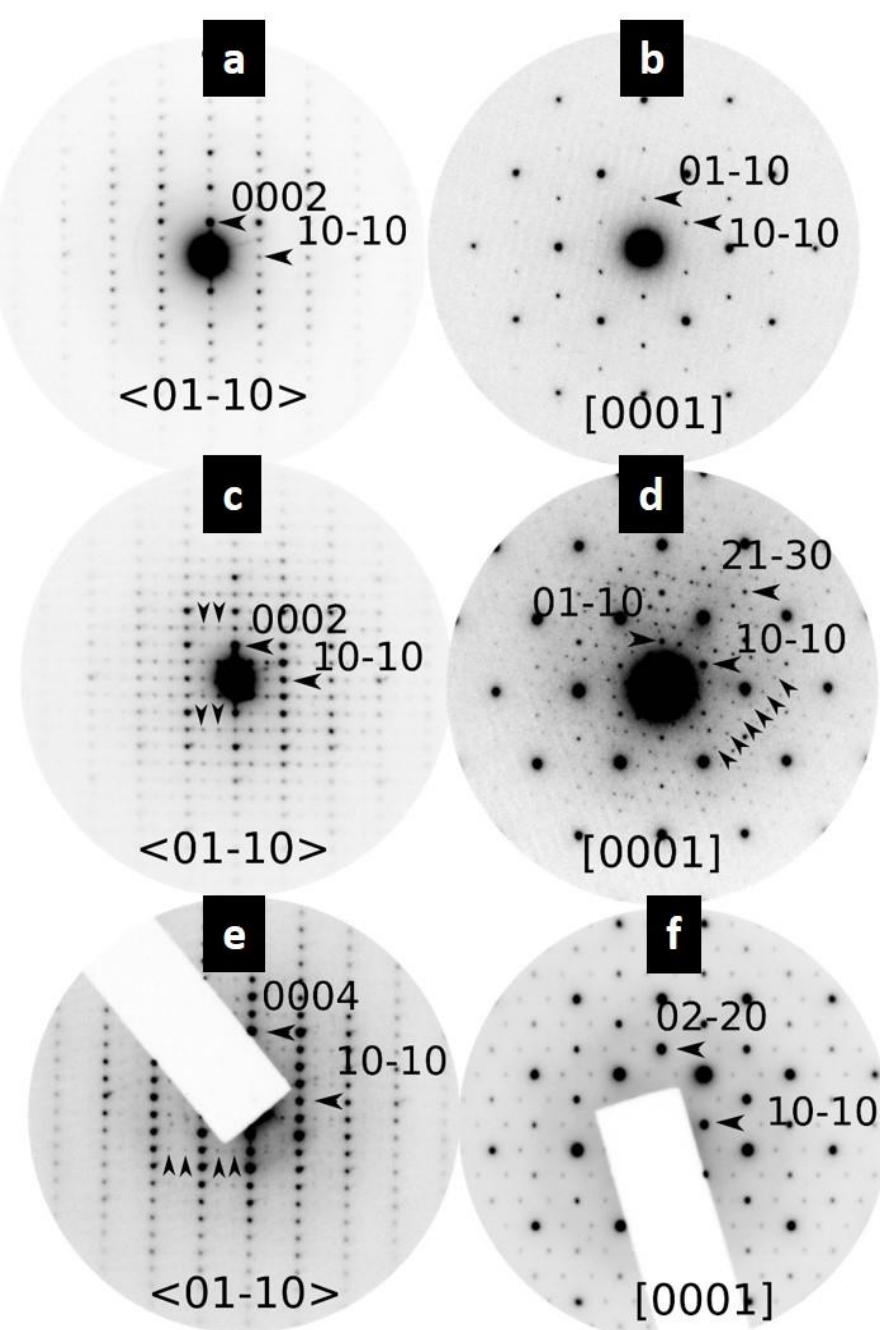


Figure 7. Collection of electron diffraction patterns recorded at different temperatures by using a heating stage in the electron microscope. The patterns in a) and b) are found at room temperature. After a few minutes at this 523 K, the patterns are transformed into the ones presented in c) and d). Finally, e) and f) are the patterns corresponding to the same crystals oriented down the same directions as before. In all cases, indexation is done according to the basic 6H structure type.

1
2
3
4
Table 1. Data for CO oxidation: temperature values for $T_{50\%}$ conversion to CO_2 for fresh 6H-BaFeO_{2.78} and
5 when is pretreated at 523 and 623 K in 5 % H₂/Ar.

Sample	Pretreatment	$T_{50\%}$ (K)
6H-BaFeO _{2.78}	523K/O ₂	618
	523K/H ₂	664
	623K/H ₂	679